UC Davis
UC Davis Previously Published Works

Title

Defects and Strain Accommodation in Epitaxial La 0.7 Sr 0.3 MnO 3 /La 0.7 Sr 0.3 CoO 3 Heterostructures

Permalink

https://escholarship.org/uc/item/58g1h5n1

Journal

Microscopy and Microanalysis, 22(S3)

ISSN

1431-9276

Authors

Byers, J Paige
Malik, Vivek K
Li, Binzhi
et al.

Publication Date

2016-07-01

DOI

10.1017/s1431927616010035

Peer reviewed

Correlation between epitaxial strain and magnetic properties in $La_{0.7}Sr_{0.3}CoO_3/La_{0.7}Sr_{0.3}MnO_3$ bilayers

J. Paige Byers, Binzhi Li, Rajesh V. Chopdekar, Jeffrey Ditto, David C. Johnson, Yayoi Takamura, and Nigel D. Browning

Correlation between epitaxial strain and magnetic properties in La₀.₇Sr₀.₃CoO₃/La₀.₇Sr₀.₃MnO₃ bilayers
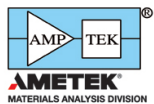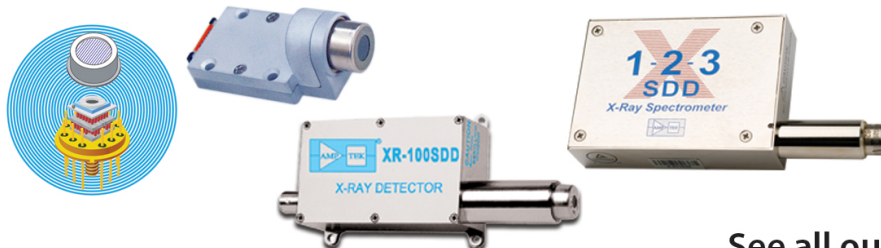
J. Paige Byers,[1] Binzhi Li,[1] Rajesh V. Chopdekar,[1,a] (iD) Jeffrey Ditto,[2] David C. Johnson,[2] Yayoi Takamura,[1,b] (iD)
and Nigel D. Browning[3,c]

AFFILIATIONS

[1] Department of Materials Science and Engineering, University of California, Davis, Davis, California 95616, USA
[2] Department of Chemistry, University of Oregon, Eugene, Oregon 97403, USA
[3] Physical and Computational Science Directorate, Pacific Northwest National Laboratory, Richland, Washington 99354, USA

[a] Present address: Advanced Light Source, Lawrence Berkeley National Laboratory, Berkeley, California 94720, USA.
[b] ytakamura@ucdavis.edu
[c] Present address: Department of Mechanical, Materials, and Aerospace Engineering, University of Liverpool, Liverpool L69 3BX, United Kingdom. nigel.browning@liverpool.ac.uk

ABSTRACT

Magnetic properties arising at interfaces of perovskite oxides such as La₀.₇Sr₀.₃CoO₃ (LSCO) and La₀.₇Sr₀.₃MnO₃ (LSMO) depend sensitively on the fine details of their structural properties. In this work, we use high-resolution transmission electron microscopy and spectroscopy to examine the structural and electronic phenomena at the interfaces in two LSCO/LSMO bilayers with reversed growth order. Two different strain mechanisms are at work in these films: compressive or tensile epitaxial strain, and distortion of the octahedral tilt pattern to maintain a network of corner-sharing octahedra. While the epitaxial strain is constant regardless of the growth order, the modification of the octahedral tilt pattern depends on whether the film is grown directly on the substrate or as the second sublayer. As a consequence, exchange spring behavior is observed only when the LSCO sublayer is grown first. The different mechanisms of strain accommodation within the oxygen octahedra network in each material proved to be of critical importance in determining the interfacial structure and thus magnetic and electronic properties of the bilayers.

Published under license by AIP Publishing. https://doi.org/10.1063/1.5054003

I. INTRODUCTION

Transition metal ABO₃ perovskites continue to be the subject of research not only due to the wide range of magnetic, electronic, and ferroelectric properties they possess but also because these properties can be tuned through manipulation of multiple lattice, spin, orbital, and charge degrees of freedom.[1–4] The structure has a wide compositional flexibility for various dopants on the A or B sites as well as the oxygen stoichiometry. This flexibility combined with the ability to precisely control thin film growth allows for the rational design of new artificial composite materials with emergent functional properties at interfaces, which are markedly different from those of their bulk counterparts.[1–6] Interfacial interactions include epitaxial strain, charge transfer, or magnetic exchange interactions, and they have the

potential for use in a wide range of applications. An important phenomenon in areas such as data storage, magnetic memory, and high performance permanent magnets is exchange bias, which involves interfacial exchange coupling between ferromagnetic/antiferromagnetic (FM/AFM) and hard FM/soft FM materials.[7–9] At these interfaces, the AFM or hard FM layer will pin the direction of the magnetization of the soft FM layer. This pinning results in a hysteresis loop that is shifted antiparallel to the original biasing field. In FM/FM coupling, the combination of a hard FM material with high coercivity and a soft FM material with high saturation magnetization results in permanent magnets in which the maximum energy product, $(BH)_{max}$, is optimized.[9–11] The majority of studies into exchange-spring behavior have been focused on metallic systems; however, the perovskites

present versatile alternatives to controlling interfacial magnetic behavior.

Previous work on bilayers of magnetically hard FM $La_{0.7}Sr_{0.3}CoO_3$ (LSCO) and magnetically soft FM $La_{0.7}Sr_{0.3}MnO_3$ (LSMO) observed exchange spring behavior when the LSCO layer was grown directly on the $(LaAlO_3)_{0.3}(Sr_2AlTaO_6)_{0.7}$ (LSAT) substrate and its thickness was above a critical thickness of ~5 nm.[12,13] A horizontal shift of the biased hysteresis loops demonstrated that the hard LSCO layer pinned the moments of the soft FM layer. Soft x-ray magnetic spectroscopy showed that this soft FM layer was composed of the LSMO layer as well as an interfacial LSCO sublayer with magnetically active Co^{2+} ions. This magnetic coupling was attributed to charge transfer across the LSCO/LSMO interface, resulting in a higher Mn^{4+}/Mn^{3+} ratio in the LSMO layer in the vicinity of the interface. However, when the bilayer stacking order was reversed so that the LSMO layer was in direct contact with the LSAT substrate, the exchange spring behavior was not observed.[14] As the misfit strain in the two bilayers remains the same, these results suggest that an additional mechanism dictates the interfacial magnetic and electronic properties, thus motivating the examination of the structural and electronic character of the bilayers with atomic scale resolution using scanning transmission electron microscopy (STEM) and spectroscopy.

Ferromagnetic and electrical properties in LSMO and LSCO develop through the double exchange mechanism[15,16] involving B–O–B chains between corner-sharing BO_6 octahedra. This double exchange mechanism also results in coincident FM/paramagnetic and metal/insulator transitions at the Curie temperature. These interactions are sensitive to both the B–O–B bond angle and bond length, and thus the magnetic and electrical properties can be manipulated by strain and coherent substrate bonding effects that introduce tilts, distortions, and rotations in the octahedral network.[2,17–22,29]

When grown epitaxially on (001)-oriented LSAT substrates, density functional theory (DFT) calculations[17] and extended x-ray absorption fine structure measurements[23] have shown that the bulk LSMO tilt pattern ($a^-a^-a^-$ in Glazer notation[24,25] with pseudocubic (pc) lattice parameter $a_{pc} = 3.873$ Å[26,27]) changes to the $a^+b^-c^-$ tilt pattern at the interface in order to accommodate strain and maintain continuity with the octahedral network in the cubic LSAT substrate which does not display octahedral tilts. In the interface region, the B–O–B bond angles also change from about 166° in all directions to close to 180° in the out-of-plane direction and about 157° in the two in-plane directions. Interestingly, some researchers report that the epitaxial distortion to the $a^+a^-c^-$ tilt pattern exists only over a few unit cells from the LSMO/LSAT interface, before returning to a more bulk-like pattern,[17] possibly facilitated by the tendency of the Mn^{3+}-O_6 octahedra to undergo Jahn-Teller (J-T) distortions.[17,19,28]

LSCO does not have J-T active oxygen octahedra; thus, epitaxial misfit strain in thin films induces changes to the octahedral tilt pattern that can persist to larger film thicknesses than in LSMO thin films.[18,30] DFT calculations showed that misfit strain and octahedral pattern distortion independently break the degeneracy of the e_g and t_{2g} orbitals,

resulting in reduced magnetization in comparison to bulk LSCO, but a combination of both effects partially restore degeneracy in two of the t_{2g} states. This behavior increased the number of unpaired spins and minimized the loss of magnetization.[18] When grown on LSAT substrates (epitaxial strain ~1% and growth plane with $a = b$), tilts in $La_{0.5}Sr_{0.5}CoO_3$ thin films were almost fully suppressed and remained so through the entire 10 nm film thickness. DFT calculations indicated that on LSAT substrates, the lowest energy state and highest magnetization is achieved when the tilt pattern was $a^0b^-c^-$.[18]

In the $La_{1-x}Sr_xCoO_3$ system, the room temperature bulk structure has rhombohedral symmetry with the $a^-a^-a^-$ tilt pattern for $0 \le x \le 0.5$ and for $x = 0.3$, the pseudocubic lattice parameter is 3.844 Å.[27,31–33] At low Sr doping, bulk $La_{1-x}Sr_xCoO_3$ exists as a spin-glass with magnetoelectronic phase separation (MEPS) where small FM clusters are isolated within an AFM matrix. At $x > 0.18$, the FM clusters coalesce leading to the evolution of FM behavior.[32,34] In thin films, MEPS was found to persist for $x > 0.18$, when the film thickness was below a critical thickness $t*$.[35] For $La_{1-x}Sr_xCoO_3$ ($x \sim 0.28$) thin films grown on $SrTiO_3$ (STO) substrates with 1.8% tensile strain, $t*$ was found to be 15 nm, while $t*$ reduced to ~8 nm when grown on LSAT substrates with 0.6% tensile strain.[36] Ordered oxygen vacancies have been observed in STEM high angle annular dark field (HAADF) images of $La_{1-x}Sr_xCoO_3$ films. The direction of this ordering relative to the substrate interface depended on epitaxial strain and substrate orientation.[37,38]

II. EXPERIMENTAL METHODS

In this work, LSCO/LSMO bilayers with an alternating growth order were grown on (001)-oriented LSAT substrates by pulsed laser deposition using a KrF excimer laser (248 nm wavelength). With a uniform Sr-concentration in both sublayers, the polarity of the LSMO/LSAT and LSCO/LSAT interfaces is the same. The bilayer with the LSCO sublayer grown first is referred to as bilayer CM, while the bilayer with the LSMO sublayer grown first is referred to as bilayer MC. During growth, the substrate temperature was held at 700 °C and the oxygen pressure was 0.3 Torr. Laser energies of 0.8 J/cm² and 1.0 J/cm², at a frequency of 5 Hz, were used for the LSMO and LSCO sublayers, respectively. To assure the proper oxygen stoichiometry, the bilayers were slowly cooled to room temperature in 300 Torr oxygen pressure after the growth.[12,13] X-ray diffraction and x-ray reflectivity (XRR) measurements were performed using a Bruker D8 Discover four-circle diffractometer with $Cu_{K\alpha1}$ x-rays. Bulk magnetization was studied using a Quantum Design superconducting quantum interference device (SQUID) magnetometer with the magnetic field applied along the in-plane [100] substrate direction. The diamagnetic signal from the LSAT substrate was subtracted, and the signal was normalized to the total thickness of the bilayer. Thin cross-section lamellae were prepared on an FEI Helios Nanolab™ 600 Dual-Beam™ focused ion beam (FIB) using wedge pre-milling methods. STEM HAADF and bright field (BF) imaging was performed in the Environmental Molecular Sciences Laboratory (EMSL) at

the Pacific Northwest National Laboratory (PNNL), using the JEOL 200CF Atomic Resolution Microscope (ARM) running at 200 kV and 15 μA. Electron energy loss spectroscopy (EELS) analysis was performed with a Gatan digital imaging system, also on the JEOL 200CF ARM. Octahedral tilts from annular bright field (ABF) images were measured using Inkscape open-source professional quality vector graphics software (https://inkscape.org).

III. RESULTS AND DISCUSSION

The layer thicknesses for both of the bilayers were determined by EELS measurements to be 16.9 ± 0.6 nm for the LSCO sublayer and 19.8 ± 0.6 nm for the LSMO sublayer, while XRR measurements of the two samples gave the total thickness for each bilayer as 37.5 ± 0.5 nm. Figure 1 shows the magnetic hysteresis loops of bilayers CM and MC as measured using a superconducting quantum interference device (SQUID) magnetometer at 80 K. Both major loops [Figs. 1(a) and 1(c)] with a maximum field of ± 24 kOe and biased minor loops [Figs. 1(b) and 1(d)] are plotted. For the biased minor loop measurements, the samples were first saturated in a field of ± 14 kOe, well above the coercive field of the hard layer, and then loops were acquired with a maximum field of ± 4 kOe, which was sufficient to switch only the soft layer. The major loops show two magnetic transitions characteristic of

heterostructures composed of two materials with different coercivities that switch independently of one another, i.e., the hard LSCO layer and soft LSMO layer. The saturation magnetization, M_S, of bilayer MC correspond well to the expected value based on the individual layer thicknesses and the bulk M_S values of LSCO ($\sim$150 emu/cm^3) and LSMO ($\sim$600 emu/cm^3).[34,39] In contrast, M_S for bilayer CM represents a 22% increase over the expected value, suggesting a substantial change in the structural properties of the bilayer. In thinner bilayers, magnetically active Co^{2+} ions with significantly higher magnetic moment per Co ion were detected from soft x-ray magnetic spectroscopy.[13] Their presence in bilayer CM could partially explain the large M_S value. Further indications of structural differences resulting from the growth order can be seen in the biased minor loops shown in Figs. 1(b) and 1(d). While both bilayers CM and MC show a vertical shift in the magnetization due to the fact that the hard LSCO layer remains magnetized along the initial biasing field direction, the loops differ in their shape, coercivity, and the fact that a horizontal shift (80 Oe) is observed only in bilayer CM where the LSCO layer was grown first [Fig. 1(d)]. This horizontal shift results from pinning of the magnetically soft layer by the adjacent hard LSCO layer. In prior work, it was found that the soft layer is composed not only of the soft LSMO layer but also of an interfacial LSCO sublayer characterized by magnetically active Co^{2+} ions.[12,13] The change in coercivity and shape of the biased minor loops
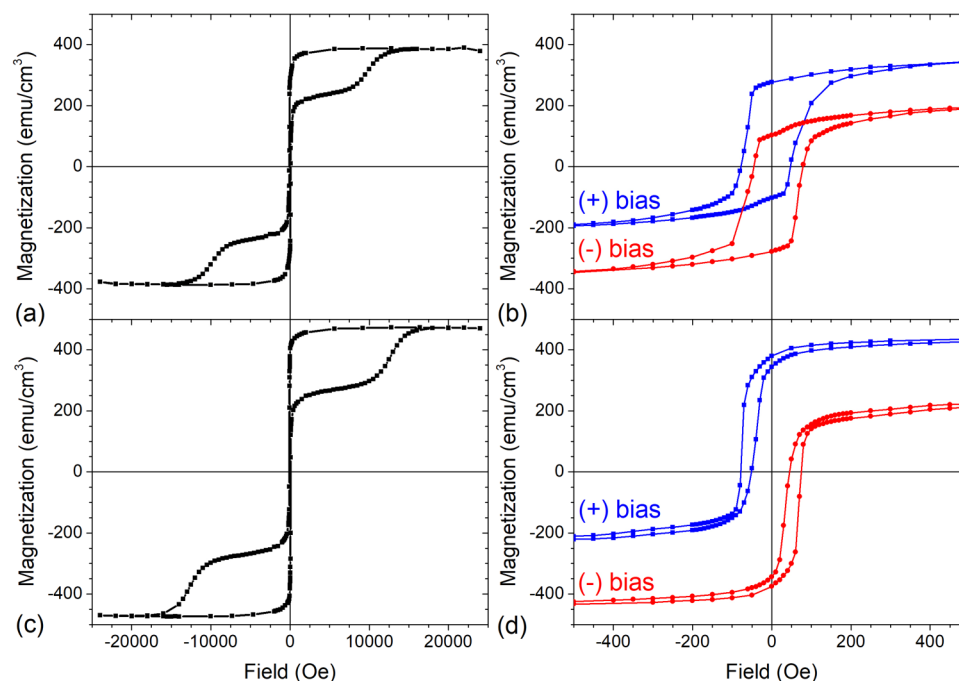
FIG. 1. Major [(a) and (c)] and biased minor [(b) and (d)] hysteresis loops measured using a SQUID magnetometer for [(a) and (b)] bilayer MC and [(c) and (d)] bilayer CM. For the biased minor loops, the samples were first biased in a field of ± 14 kOe, and loops were measured with a maximum field of ± 4 kOe, which was sufficient to only switch the soft layer.

suggests that the growth order impacts the defect density in the bilayers, as well as modifies the magnetic easy axes of the LSMO and LSCO layers. Berndt et al.[40] found that a small tensile strain (as imposed from STO substrates) can change the magnetic easy axis of LSMO films to the in-plane <110> directions, while LSCO and LSMO thin films grown on LSAT substrates as well as LSCO/LSMO superlattices with small sublayer thickness were found to have nearly equal anisotropy along the in-plane <100> and <110> directions.[41,42]

In order to compare the structure and electronic character of the bilayers with different growth orders, they were imaged with high spatial resolution using STEM. HAADF and BF images (Figs. 2 and S2 in the supplementary material) show the high crystalline quality of both bilayers, with fully coherent lattices free from dislocations and with smooth substrate interfaces. X-ray diffraction reciprocal space maps (Fig. S1 in the supplementary material) verify the lattice coherency of the bilayers to the underlying LSAT substrate. Fast Fourier transforms (FFTs) of the HAADF images (insets in Fig. S2 in the supplementary material) show that the in-plane lattice parameter was constant throughout the film thickness in both bilayers, matching the lattice parameter of the LSAT substrate (0.3868 nm). The out-of-plane lattice parameters of the LSCO and LSMO sublayers were, respectively, found to be 0.382 ± 0.050 nm and 0.389 ± 0.050 nm in bilayer CM, and 0.381 ± 0.050 nm and 0.390 ± 0.050 nm in bilayer MC, which is

consistent with those measured by x-ray diffraction.[12] In bilayer MC, the FFTs for both the LSMO and LSCO sublayers show weak diffraction spots (indicated with red circles) between the main diffraction peaks. These extra diffraction spots appear more prominently in the LSMO sublayer over the LSCO sublayer. These extra peaks are expected from rhombohedral perovskites with the $a^- a^- a^-$ tilt structure when viewed along the $[110]_{pc}$ zone axis, though they should not appear when viewed along the $[1\bar{1}0]_{pc}$ direction. For this reason, the lack of extra diffraction spots in bilayer CM alone cannot be used to rule out the occurrence of the $a^- a^- a^-$ tilt pattern.

In HAADF, the image contrast is proportional to atomic mass or sample thickness, while BF images are formed from diffraction contrast, which is more strain sensitive.[43] In bilayer MC, we observe a contrast variation at the LSMO/LSAT interface in both HAADF and BF STEM images (Figs. 2 and S3 in the supplementary material) viewed along both the <100> and <110> zone axes. The uniform in-plane lattice parameter throughout the film thickness indicates that the bilayer is fully strained, so we speculate that the strain contrast in the BF images could be attributed to distortions of the MnO_6 octahedra in the first few unit cells. These distortions maintain the corner-sharing oxygen network across the substrate-film interface, locally causing higher strain due to the absence of tilts in the cubic LSAT substrate. High strain and octahedral distortions can lead to shifts in atomic positions or point defects within atomic columns, which could cause the coincident change in contrast in the HAADF images. On the other hand, images of bilayer CM show uniform contrast across the LSAT/LSCO interface. A simple explanation for this behavior would be a scenario where the CoO_6 octahedral tilts are suppressed throughout the LSCO sublayer, as was previously reported for LSCO films grown on LSAT substrates.[18] In such a case, the LSCO sublayer should present a similar growth surface for the LSMO sublayer as a bare LSAT substrate. However, the LSMO/LSCO interface in bilayer CM lacks the contrast variation observed in the LSMO/LSAT interface in bilayer MC. Therefore, we propose an alternative structural model based on a detailed analysis of the HAADF and ABF images as described below.

Figure 3 shows HAADF and ABF images of the LSCO sublayer of bilayer CM viewed along the [110] zone axis. As with BF imaging, ABF imaging is largely diffraction contrast; however, by using an annular detector which blocks some of the signals from the more strongly diffracting A and B cations, oxygen atoms can more readily be distinguished. A distinct pattern in the oxygen ion positions can be observed in the ABF image as one moves parallel to the LSCO/LSAT interface. Specifically, the oxygen ion columns in the octahedra shift alternatively up/down with rotation around the [110] axis. The magnitude of the tilts was measured by rendering the octahedra as they would appear in the (110) plane as a stick drawing, and overlaying the drawing on the ABF image. The octahedra are then rotated, 0.5° at a time, until the vertices of the octahedra lie in the center of the oxygen columns in the ABF image. Rotation counter clockwise was defined as positive and clockwise as
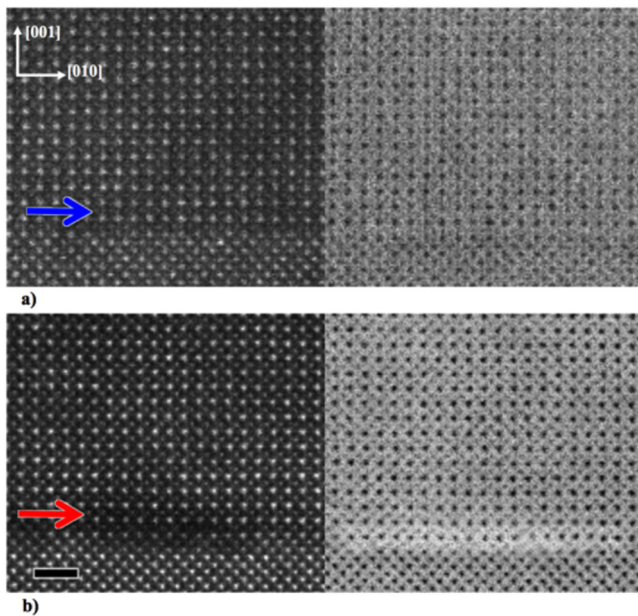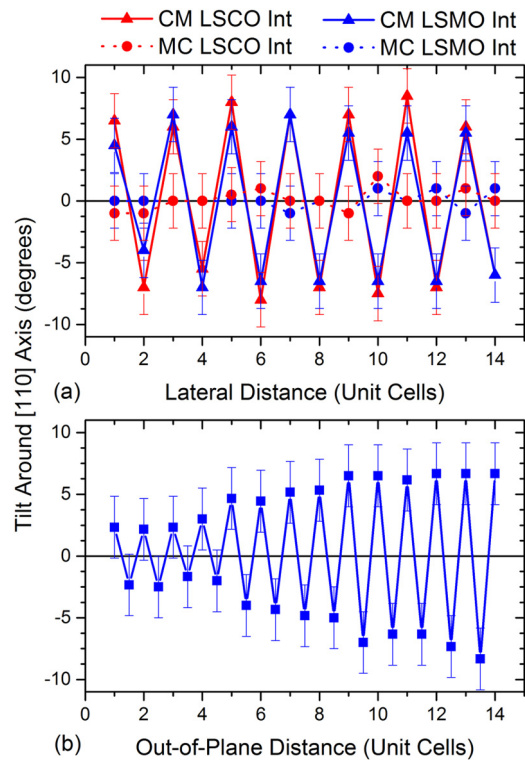
FIG. 2. HAADF and BF images viewed down the [100] zone axis of the substrate interface of (a) bilayer CM and (b) bilayer MC. Homogeneous contrast is observed at the LSCO/LSAT interface [blue arrow in (a)], but at the LSMO/LSAT interface [red arrow in (b)], the first 1–2 unit cells of LSMO show contrast variations absent in the rest of the layer. Black scale bar under image (b) is 1 nm.
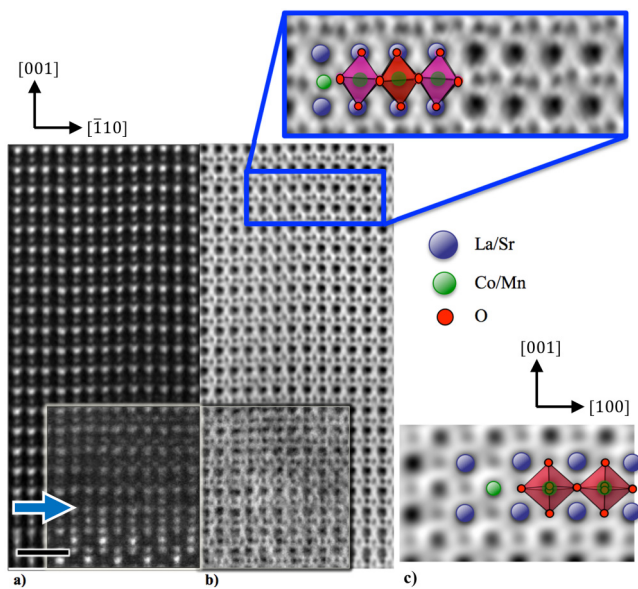
FIG. 3. (a) HAADF and (b) ABF images viewed along the [110]-zone axis of bilayer CM in the region near the LSCO/LSAT interface. The insets are the raw images, while the larger images have been noise reduced using a mask on the image FFT in Digital Micrograph. The black scale bar at the bottom of the HAADF image is 1 nm. The blue arrow denotes the location of the LSCO/LSAT interface. (c) ABF image viewed down the [100] zone axis. Models of the atomic positions corresponding to the $a^+b^-c^*$ tilt pattern with $\alpha = 1°$, $\beta = -5°$, and $\gamma = 0°$ are shown in the enlarged images of (b) and (c). Pink and red octahedral represent alternating octahedral through the lamellae thickness.


FIG. 4. Tilt angle of the oxygen network at the LSCO/LSMO interfaces (Int.) in bilayer CM (solid lines) and bilayer MC (dotted lines), along the (a) lateral and (b) out-of-plane direction relative to the LSAT interface. Tilts for [110]-oriented oxygen octahedra in (a) were measured across 14 unit cells in the [$\bar{1}$10] direction as shown in the enlarged section of Fig. 3. For (b), six octahedra in the [$\bar{1}$10] direction were measured in each monolayer, and the average positive and negative tilts were recorded.

negative. An example model with tilts of $\alpha = 1°$ and $\beta = -5°$ in an $a^+b^-c^*$ tilt pattern fits well with ABF images taken along the [110] and [100] zone axes of the LSCO sublayer in bilayer CM [Fig. 3(b), enlarged section, and Fig. 3(c)]. In order to properly represent true STEM lamellae with finite thickness, the model also accounts for the possibility of alternating octahedral tilts (represented as pink and red octahedra in Fig. 2) through the lamellae thickness. Figures S4(a) and S4(b) in the supplementary material show that the alternating pattern of octahedral tilts around the [110] axis is continuous across the LSCO/LSMO interface and persists into the first several unit cells of the LSMO sublayer. The images taken along the [100] zone axis [Figs. 3(c) and S4(b) in the supplementary material] show that tilts in at least one in-plane principal direction are either in-phase or that the tilts are too small to be differentiated with the available data. The latter case is not consistent with the pattern observed in images viewed along the [110] zone axis. Modeling then proceeded under the assumption that tilts around the x-axis (α) are in-phase and relatively small. With the alternating pattern in the [110] zone axis images, tilts around the y-axis (β) were assumed to be out-of-phase, and larger than α in order to cause the significant rotations measured. The c^* indicates that any rotation around the [001] direction is undetermined, and for this analysis is assumed to be c^0.

Figure 4(a) plots the magnitude of the octahedral tilts obtained from the LSCO/LSMO interface in both bilayers CM and MC, while Fig. S5 in the supplementary material separately shows the octahedral tilts extracted from the substrate interface (substrate), the LSCO/LSMO interface (interface), and from the middle of the sublayer (middle). The average rotations for each region of the bilayer are also shown with 2σ error bars. When the alternating pattern exists, the average positive and negative measurements are reported separately. From this set of data, we can see that the alternating pattern in the octahedral tilts is observed only in bilayer CM. Finally, Fig. 4(b) plots the magnitude of the octahedral tilts in the LSCO sublayer of bilayer CM as a function of position in the growth direction (i.e., perpendicular to the substrate interface). The magnitude of the tilts in the LSCO sublayer starts at a value of $3°-5° \pm 2.2°$ at the LSCO/LSAT interface and gradually increases to a value of $6°-10° \pm 2.2°$ after 14-16 unit cells (~5.5-6 nm). The tilts alternate vertically to maintain connectivity of the octahedra. This tilt pattern persists

across the LSCO/LSMO interface and into the LSMO sublayer; however, the magnitude decreases to ±2°-3° after 4-6 unit cells (~1.5-2 nm) past the LSCO/LSMO interface and becomes essentially zero by the middle of the LSMO sublayer [Fig. S4(b) in the supplementary material].

In bilayer MC, there are weak indications of octahedral tilts in both sublayers when viewed along the [110] zone axis, but they lack the clear regularity of those in bilayer CM, and with the calculated 2σ error bars, the average value converges to zero. In this case, the octahedral tilts likely revert to the bulk $a^-a^-a^-$ pattern by the formation of the strain-distorted region at the LSMO/LSAT interface observed in the HAADF and BF images shown in Fig. 2. This $a^-a^-a^-$ pattern is confirmed by the diagonal elongation or smearing of the oxygen columns in the ABF images. In Figs. S4(c) and S4(d) in the supplementary material, a model of this pattern demonstrates good fit with the images and shows why the oxygen columns appear drawn out, but the overall tilt observed is negligible. In contrast, the highly strained region is absent at the LSCO/LSMO interface in bilayer CM, where the $a^+b^-c^*$ from the underlying LSCO layer is able to penetrate the LSMO sublayer.

EELS was performed in a unit cell-by-unit cell fashion to probe the amount of chemical intermixing and/or charge transfer across the LSCO/LSMO interface of both bilayers. Figure 5(a) shows that chemical intermixing of Mn and Co ions in bilayer CM is limited to a distance of ±0.3-0.4 nm (<one unit cell). Similar results were obtained for bilayer MC. By reducing the chromatic range of the inelastically scattered electrons that are collected, the energy resolution can be improved such that small changes in a spectrum's fine structure can be detected. Energy loss near edge structure can give information on the oxidation state and bonding environment. Energy shifts, peak ratios, or peak shapes can be examined and for some elements, related to the electronic state.[44,45] The Co-EELS spectra taken from regions near the LSCO/LSMO interface *vs.* the middle of the sublayer of bilayer CM [Fig. 5(b)] show that the intensities of the two Co L-edge white lines, i.e., L_3/L_2 peak intensity ratios are markedly different: 1.54 at the interface compared to 2 in the middle of the sublayer. This difference indicates a change in the average Co oxidation state at the interface from $Co^{3+/4+}$ to Co^{2+}, as was detected in thinner bilayers by soft x-ray magnetic spectroscopy.[12,13] This result is consistent with a charge transfer across the interface. The O K-edge spectra from the same areas show a significantly muted excitation peak at the LSCO/LSMO interface [Fig. 5(c)]. Electrons transferring to the Co ions, which are bonded with oxygen ions in the interfacial LSCO region, cause a decrease in the number of unoccupied states in both elements for electrons excited by the electron beam, resulting in a decrease in intensity of the excitation peak.[44,46] In contrast, comparing spectra from bilayer MC, shown in Fig. S6 in the supplementary material, the L_3/L_2 peak intensity ratios for both Co and Mn ions are essentially identical at the interface and in the middle of the layer. For Mn, these ratios are 2.13 (interface) and 2.0 (middle), corresponding to mixed $Mn^{3+/4+}$ ions, and
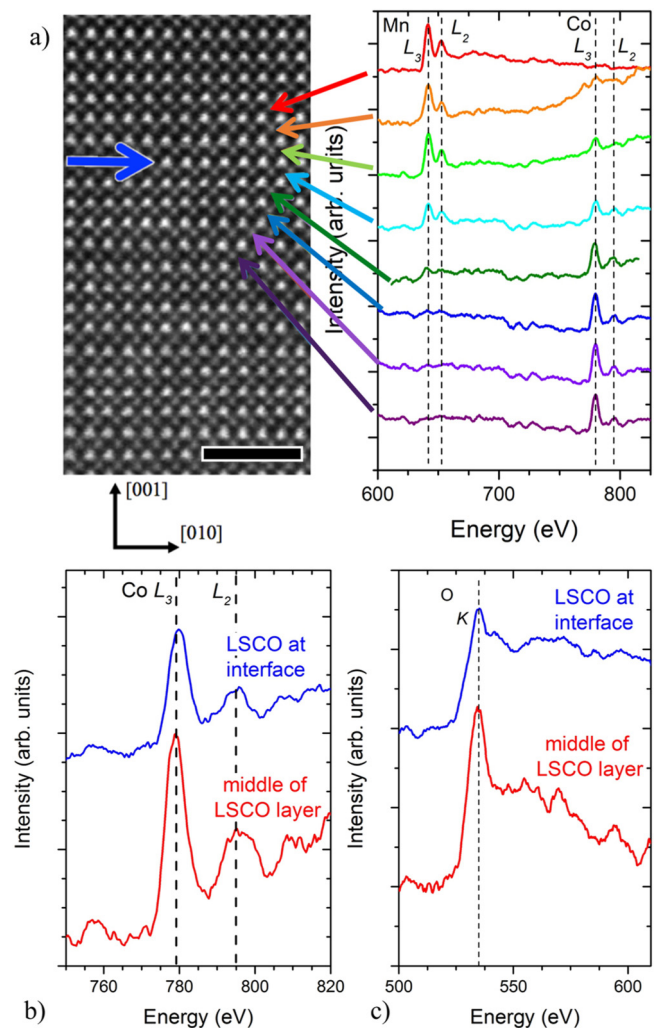
FIG. 5. (a) HAADF images of bilayer CM at the LSCO/LSMO interface (blue arrow); (b) Co EELS spectra and (c) oxygen EELS spectra the LSCO/LSMO interface region and the middle of the LSCO layer. The vertical dotted lines on the plots indicate the energy of the Mn L_3/L_2, Co L_3/L_2, and O K-edge white lines. The Co L_3/L_2 peak ratio at the LSCO/LSMO interface = 1.54, while at the middle of the LSCO layer L_3/L_2 = 2. Black scale bar in (a) is 2 nm.

for Co, the ratios are 1.9 (interface) and 2.0 (middle), consistent with mixed $Co^{3+/4+}$ ions.

The STEM imaging and EELS measurements have shown that the growth order for the LSCO/LSMO bilayers has a profound influence on the structural properties of the individual layers which goes beyond tetragonal distortion due to epitaxial strain. ABF imaging shows that the response of the oxygen octahedral network within the first few unit cells at the LSAT interface differs, which ultimately affects the overall electronic and magnetic properties of the bilayer, including the presence or absence of the exchange spring

behavior. In bilayer CM where the LSCO sublayer is grown directly on the LSAT substrate, a robust, alternating pattern of octahedral tilts consistent with an $a^+b^-c^*$ tilt pattern was observed throughout the LSCO sublayer, extending at least 4–6 unit cells into the LSMO layer. This connectivity of the oxygen octahedral network may facilitate a $Mn^{3+} + Co^{3+} \leftrightarrow Mn^{4+} + Co^{2+}$ charge transfer across the LSCO/LSMO interface, and thus the formation of the interfacial LSCO layer with magnetically active Co^{2+} ions which are coupled magnetically to the soft LSMO layer. As a result, this bilayer exhibits an exchange spring behavior where the hard LSCO sublayer biases the soft FM layer such that the hard/soft interface lies within the LSCO layer. Furthermore, the measured M_S value for bilayer CM is ~22% higher than expected based on bulk M_S values. While the presence of the magnetically active Co^{2+} ions at the LSCO/LSMO interface could be partially responsible, the small thickness of the interfacial layer makes it unlikely to be the sole cause. Rather the observed epitaxial strain in combination with the distorted tilt structure may lead to a change in the electronic bandwidth of the perovskite structure[26,47] and therefore an enhancement in the magnetization of all layers in the bilayer. A similar enhancement in magnetization and Curie temperature has been reported for $La_{0.5}Sr_{0.5}CoO_3$ films on (101)-oriented orthorhombic $NdGaO_3$ substrates[18] as well as δ-doped $La_{0.5}Sr_{0.5}MnO_3$ layers on LSAT substrates,[48] and LSMO/$Eu_{0.7}Sr_{0.3}MnO_3$ superlattices on LSAT substrates.[49]

In bilayer MC, the epitaxial strain in the LSMO sublayer is accommodated within the first 1–2 unit cells such that the remainder of the LSMO sublayer is characterized by bulk-like $a^-a^-a^-$ tilts. This case presents a markedly different growth surface for the LSCO sublayer, compared to when it is grown directly on the LSAT substrate. In turn, the $a^+b^-c^*$ pattern does not develop in the LSCO sublayer of bilayer MC. This oxygen octahedral network results in decoupled magnetic layers with the expected bulk-like M_S values, and which lack both charge transfer across the LSCO/LSMO interface and the exchange spring behavior observed in bilayer CM.

In summary, with high resolution electron microscopy, we offer evidence that the BO_6 octahedra in LSCO and LSMO layers grown epitaxially on LSAT substrates exhibit differing responses to epitaxial strain and substrate coherency. The ability of the epitaxially strained LSCO sublayer to maintain an $a^+b^-c^*$ octahedral tilt pattern throughout the full film thickness (~20 nm), which then extends into the LSMO sublayer, directly impacts the electronic and magnetic properties of the LSCO/LSMO bilayer. This system exhibits charge transfer across the LSCO/LSMO interface, exchange spring behavior, and an enhanced saturation magnetization. In contrast, when the LSMO sublayer is grown directly on the LSAT substrate, the epitaxial strain is largely accommodated within 1–2 unit cells of the substrate interface and the bilayer behaves as decoupled magnetic layers. These findings highlight the importance of building fundamental models to predict the mechanisms of strain accommodation, and the resulting electronic and magnetic properties.

SUPPLEMENTARY MATERIAL

See supplementary material for additional x-ray diffraction data, STEM images, and EELS spectra.

REFERENCES

[1]P. Zubko, S. Gariglio, M. Gabay, P. Ghosez, and J.-M. Triscone, Annu. Rev. Condens. Matter Phys. **2**, 141 (2011).
[2]A. Bhattacharya and S. J. May, Ann. Rev. Mater. Res. **44**, 65 (2014).
[3]J. Chakhalian, J. W. Freeland, A. J. Millis, C. Panagopoulos, and J. M. Rondinelli, Rev. Mod. Phys. **86**, 1189 (2014).
[4]H. Y. Hwang, Y. Iwasa, M. Kawasaki, B. Keimer, N. Nagaosa, and Y. Tokura, Nat. Mater. **11**, 103 (2012).
[5]A. Ohtomo and H. Y. Hwang, Nature **427**, 423 (2004).
[6]H. Yamada, Y. Ogawa, Y. Ishii, H. Sato, M. Kawasaki, H. Akoh, and Y. Tokura, Science **305**, 646 (2004).
[7]J. Nogues and I. K. Schuller, J. Magn. Magn. Mater. **192**, 203 (1999).
[8]W. H. Meiklejohn and C. P. Bean, Phys. Rev. **102**, 1413 (1956).
[9]E. E. Fullerton, J. S. Jiang, and S. D. Bader, J. Magn. Magn. Mater. **200**, 392 (1999).
[10]R. Skomski and J. M. D. Coey, Phys. Rev. B **48**, 15812 (1993).
[11]E. F. Kneller and R. Hawig, IEEE Trans. Magn. **27**, 3588 (1991).
[12]B. Li, R. V. Chopdekar, E. Arenholz, A. Mehta, and Y. Takamura, Appl. Phys. Lett. **105**, 202401 (2014).
[13]B. Li, R. V. Chopdekar, A. T. N'Diaye, A. Mehta, J. P. Byers, N. D. Browning, E. Arenholz, and Y. Takamura, Appl. Phys. Lett. **109**, 152401 (2016).
[14]R. V. Chopdekar, V. K. Malik, A. M. Kane, A. Mehta, E. Arenholz, and Y. Takamura, J. Phys. Condens. Mater. **30**, 015805 (2018).
[15]P. W. Anderson and H. Hasegawa, Phys. Rev. **100**, 675 (1955).
[16]C. Zener, Phys. Rev. **82**, 403 (1951).
[17]E. J. Moon, P. V. Balachandran, B. J. Kirby, D. J. Keavney, R. J. Sichel-Tissot, C. M. Schlepütz, E. Karapetrova, X. M. Cheng, J. M. Rondinelli, and S. J. May, Nano Lett. **14**, 2509 (2014).
[18]M. D. Biegalski, Y. Takamura, A. Mehta, Z. Gai, S. V. Kalinin, H. Ambaye, V. Lauter, D. Fong, S. T. Pantelides, Y. M. Kim, J. He, A. Borisevich, W. Siemons, and H. M. Christen, Adv. Mater. Interfaces **1**, 1400203 (2014).
[19]A. Y. Borisevich, H. J. Chang, M. Huijben, M. P. Oxley, S. Okamoto, M. K. Niranjan, J. D. Burton, E. Y. Tsymbal, Y. H. Chu, P. Yu, R. Ramesh, S. V. Kalinin, and S. J. Pennycook, Phys. Rev. Lett. **105**, 087204 (2010).
[20]I. Solovyev, N. Hamada, and K. Terakura, Phys. Rev. Lett. **76**, 4825 (1996).
[21]Y. Takamura, R. V. Chopdekar, E. Arenholz, and Y. Suzuki, Appl. Phys. Lett. **92**, 162504 (2008).
[22]F. Yang, N. Kemik, M. D. Biegalski, H. M. Christen, E. Arenholz, and Y. Takamura, Appl. Phys. Lett. **97**, 092503 (2010).
[23]A. Vailionis, H. Boschker, W. Siemons, E. P. Houwman, D. H. A. Blank, G. Rijnders, and G. Koster, Phys. Rev. B **83**, 064101 (2011).

[24]A. M. Glazer, Acta Cryst. **B28**, 3384 (1972).

[25]A. M. Glazer, Acta Cryst. **A31**, 756 (1975).

[26]P. G. Radaelli, G. Iannone, M. Marezio, H. Y. Hwang, S. W. Cheong, J. D. Jorgensen, and D. N. Argyriou, Phys. Rev. B **56**, 8265 (1997).

[27]A. N. Petrov, V. I. Voronin, T. Norby, and P. Kofstad, J. Solid State Chem. **143**, 52 (1999).

[28]J. He, A. Borisevich, S. V. Kalinin, S. J. Pennycook, and S. T. Pantelides, Phys. Rev. Lett. **105**, 227203 (2010).

[29]R. Aso, D. Kan, Y. Shimakawa, and H. Kurata, Sci. Rep. **3**, 2214 (2013).

[30]N. Sundaram, Y. Jiang, I. E. Anderson, D. P. Belanger, C. H. Booth, F. Bridges, and J. F. Mitchell, Th. Proffen, and H. Zheng, Phys. Rev. Lett. **102**, 026401 (2009).

[31]A. Mineshige, M. Kobune, S. Fujii, Z. Ogumi, M. Inaba, T. Yao, and K. Kikuchi, J. Solid State Chem. **142**, 374 (1999).

[32]M. A. Senaris-Rodriguez and J. B. Goodenough, J. Solid State Chem. **118**, 323 (1995).

[33]R. Caciuffo, D. Rinaldi, G. Barucca, J. Mira, J. Rivas, M. A. Senaris-Rodriguez, P. G. Radaelli, D. Fiorani, and J. B. Goodenough, Phys. Rev. B **59**, 1068 (1999).

[34]J. Wu and C. Leighton, Phys. Rev. B **67**, 174408 (2003).

[35]M. A. Torija, M. Sharma, J. Gazquez, M. Varela, C. He, J. Schmitt, J. A. Borchers, M. Laver, S. El-Khatib, and C. Leighton, Adv. Mater. **23**, 2711 (2011).

[36]B. Li, R. V. Chopdekar, A. T. N'Diaye, E. Arenholz, and Y. Takamura, AIP Adv. **7**, 045003 (2017).

[37]W. S. Choi, J.-H. Kwon, H. Jeen, J. E. Hamann-Borrero, A. Radi, S. Macke, R. Sutarto, F. He, G. A. Sawatzky, V. Hinkov, M. Kim, and H. N. Lee, Nano Lett. **12**, 4966 (2012).

[38]J. Gazquez, S. Bose, M. Sharma, M. A. Torija, S. J. Pennycock, C. Leighton, and M. Varela, APL Mater. **1**, 012105 (2013).

[39]A. Urushibara, Y. Moritomo, T. Arima, A. Asamitsu, G. Kido, and Y. Tokura, Phys. Rev. B **51**, 14103 (1995).

[40]L. M. Berndt, V. Balbarin, and Y. Suzuki, Appl. Phys. Lett. **77**, 2903 (2000).

[41]V. K. Malik, C. H. Vo, E. Arenholz, A. Scholl, A. T. Young, and Y. Takamura, J. Appl. Phys. **113**, 153907 (2013).

[42]T. A. Wynn, B. Li, R. V. Chopdekar, A. T. N'Diaye, E. Arenholz, and Y. Takamura (unpublished).

[43]D. B. Williams and C. B. Carter, *Transmission Electron Microscopy: A Textbook for Materials Science* (Springer, New York, 2009).

[44]R. F. Egerton, *Electron Energy-Loss Spectroscopy in the Electron Microscope* (Springer, New York, 2011).

[45]G. A. Botton, MRS Bull. **37**, 21 (2012).

[46]N. Gauquelin, E. Benckiser, M. K. Kinyanjui, M. Wu, Y. Lu, G. Christiani, G. Logvenov, H.-U. Habermeier, U. Kaiser, B. Keimer, and G. A. Botton, Phys. Rev. B **90**, 195140 (2014).

[47]J. B. Goodenough, Rep. Prog. Phys. **67**, 1915 (2004).

[48]E. J. Moon, Q. He, S. Ghosh, B. J. Kirby, S. T. Pantelides, A. Y. Borisevich, and S. J. May, Phys. Rev. Lett. **119**, 197204 (2017).

[49]E. J. Moon, R. Colby, Q. Wang, E. Karapetrova, C. M. Schlepütz, M. R. Fitzsimmons, and S. J. May, Nat. Commun. **5**, 5710 (2014).